Nonplanar Nanofabrication via Interface Engineering

by

Sarah O. Spector

B.S., Massachusetts Institute of Technology (2021)

Submitted to the Department of Electrical Engineering and Computer Science
in partial fulfillment of the requirements for the degree of

Master of Science

at the

MASSACHUSETTS INSTITUTE OF TECHNOLOGY

February 2023

© Massachusetts Institute of Technology 2023. All rights reserved.

Author . . . .
Department of Electrical Engineering and Computer Science
January 25, 2023

Certified by . . . .
Farnaz Niroui
Assistant Professor of Electrical Engineering and Computer Science
Thesis Supervisor

Accepted by . . . .
Leslie A. Kolodziejski
Professor of Electrical Engineering and Computer Science
Chair, Department Committee on Graduate Students

Nonplanar Nanofabrication via Interface Engineering

by

Sarah O. Spector

Submitted to the Department of Electrical Engineering and Computer Science
on January 25, 2023, in partial fulfillment of the
requirements for the degree of
Master of Science

Abstract

This thesis develops a platform for scalable fabrication of suspended, ultrathin nanostructures as building blocks of nanoelectromechanical systems by extending conventional planar techniques to nonplanar designs. We achieve this by engineering interface forces through a patterned molecular monolayer to enable controlled delamination of a deposited thin-film in predetermined locations. This allows us to form nonplanar structures with thicknesses < 10 nm and nanogaps reaching < 10 nm – features traditionally challenging to achieve. Our approach, which builds on standard, wafer-scale, and conventionally-compatible techniques, is versatile, tunable, and compatible with diverse materials. As a result, the technique opens up new opportunities for applications such as miniaturized nanoelectromechanical devices, including ultrathin mechanical resonators, which are demonstrated in this work.

Thesis Supervisor: Farnaz Niroui
Title: Assistant Professor of Electrical Engineering and Computer Science

Acknowledgments

This work would not have been possible without the support, advice, and ideas of the fellow students in my research group, Spencer Zhu, Shelly Ben-David, Teddy Hsieh, Patricia Jastrzebska-Perfect, Lejla Skelic, and particularly Peter Satterthwaite.

I would like to give special thanks to my advisor and PI, Professor Farnaz Niroui, whose ideas were integral to every step of this project and who supported me professionally and academically all along the way.

The mechanical resonance characterization was performed by our collaborators Dr. David Czaplewski and Dr. Jian Zhou at Argonne National Laboratory, and I greatly thank them for their assistance with this measurement.

I acknowledge and thank all of the MIT.Nano fab staff for helping to wrangle the tools, particularly Kurt Broderick, Dave Terry, Dennis Ward, Bob Bicchieri, Donal Jamieson, Eric Lim, Gary Riggott, and Scott Poesse.

Finally, I thank my parents, Marcie Berger and John Spector, my roommates, An Jimenez, Kate Pearce, and Ilona Neale, and particularly my partner, Jay Hesslink, for personal support while I carried out this thesis work.

Contents

1 Introduction **9**

2 Fabrication of nanoelectromechanical systems **11**

2.1 NEMS and their applications . . . 11

2.2 Conventional methods . . . 12

2.3 Alternative techniques . . . 12

2.4 Thin-film blistering for NEMS fabrication . . . 14

3 Nonplanar nanofabrication method **16**

3.1 Technique overview . . . 16

3.2 Self-assembled molecular monolayers . . . 17

3.2.1 Introduction to SAMs . . . 17

3.2.2 Patterning of SAMs . . . 18

3.2.3 Assembly and properties of (3-aminopropyl)triethoxysilane . . . 20

3.3 Atomic layer deposition . . . 21

3.3.1 ALD chemistry . . . 21

3.3.2 ALD growth on molecules . . . 22

3.3.3 Discussion . . . 26

3.4 Controlled film buckling . . . 27

3.4.1 Thermal stress in thin films . . . 28

3.4.2 Modeling of thin film buckling . . . 29

3.4.3 Empirical results . . . 33

3.4.4 Discussion . . . 35

3.5 Material compatibility 36
3.6 Scalable fabrication of a mechanical resonator 38

4 Mechanical resonator and characterization 41
4.1 Mass spectroscopy application 41
4.2 Finite element modeling 42
4.3 Empirical characterization 44
4.4 Discussion 46

5 Conclusion and future work 48

A Fabrication parameters 50
A.1 Substrate preparation 50
A.2 Oxide hard mask 50
A.3 APTES growth and hard mask removal 51
A.4 Thin-film growth and blistering 51
A.5 Etching blisters into double-clamped beams 52

List of Figures

2-1 Limitations of conventional NEMS fabrication 13
2-2 Alternative 3D fabrication techniques 14

3-1 Fabrication technique overview 17
3-2 SAM patterning method using an Al_2O_3 hard mask 19
3-3 APTES and its thermal stability 21
3-4 Diagram of TMA/H_2O ALD 22
3-5 Literature demonstrations of SAMs used for ALD blocking 24
3-6 Reaction pathway for ALD of Al_2O_3 on an $-NH_2$ termination 25
3-7 Ellipsometric measurements of ALD on varying surfaces 27
3-8 Plot of thermal stress in an ALD Al_2O_3 film 30
3-9 Illustration of a two-dimensional circular delamination buckle 31
3-10 Diagram of geometric dimensions used in stress calculations 32
3-11 Plot of blister height vs. diameter 33
3-12 Plot of blister diameter vs. APTES size and spacing 34
3-13 Plot of average blister radius vs. APTES size + spacing 35
3-14 Plot of blistering force vs. thermal stress force 36
3-15 Images of recrystallized annealed metals 37
3-16 Images demonstrating the technique with different materials 38
3-17 Fabrication steps for converting the nanoblister to a bridge geometry. 39
3-18 SEM images of examples of bridge nanostructures fabricated using the discussed technique. 40

4-1 Shapes of the first four vibrational modes for the canonical blister and bridge geometries, generated in COMSOL. 43
4-2 Dependence of resonator fundamental frequency on geometric parameters, from COMSOL simulation 44
4-3 Laser interferometer setup for resonance measurement 45
4-4 Characterization of example bridge resonator 46

List of Tables

3.1 Material parameters for thin ALD Al_2O_3 and bulk Si 29

4.1 Material parameters for thin ALD Al_2O_3 used in the finite element modeling 42

Chapter 1

Introduction

The downscaling of electronic devices, including electromechanical systems with micro- and nanoscale moving parts, is necessary for the development of next-generation systems with improved energy efficiency, high sensitivity, and new functionalities. These devices will find applications in sensing, actuation, computing, and communication. However, to achieve these characteristics in nanoelectromechanical systems (NEMS), alternative fabrication techniques are required for further miniaturization. At the nanoscale, surface adhesive forces induce instabilities that render the conventional top-down processing flow of lithography, deposition, and etching insufficient.

This thesis will present a new fabrication technique where surface forces are leveraged in a directed bottom-up strategy to engineer suspended, nonplanar, ultrathin features for NEMS devices. In this approach, instead of etching away a sacrificial layer to create suspended features, we engineer interface forces and material stresses to direct the spontaneous deformation of planar materials into nonplanar geometries. In doing so, we move past the traditional paradigm of microelectronics fabrication to introduce the use of unconventional materials and techniques to enable ultrathin NEMS structures.

First, the literature on NEMS fabrication, both conventional and unconventional, will be reviewed, along with discussion on applications and desired device properties. Next, the developed technique will be presented along with background and analysis on the constituent materials and fabrication steps, and the empirical results will be

discussed and compared to theory. Finally, a potential application of the technique for fabrication of ultrathin mechanical resonators will be discussed and an example device will be demonstrated. Details of the fabrication process can be found in Appendix A.

Chapter 2

Fabrication of nanoelectromechanical systems

This chapter will discuss the context of nanoelectromechanical systems (NEMS), their uses and applications, limitations of current fabrication methods, and challenges faced by the field due to these shortcomings. Alternatives to the conventional techniques will be introduced, with special emphasis on the literature related to this thesis.

2.1 NEMS and their applications

Over many decades, microfabrication technology has been relentlessly improved and developed, primarily driven by the economic forces of Moore's Law and the huge advantages afforded to electronic transistors by miniaturization. However, this technological progress has also benefited additional types of electronic devices beyond transistors. Microelectromechanical systems (MEMS), which utilize microscale movable parts to achieve some functionality, have leveraged the same silicon-based, planar fabrication techniques to reach smaller scales and new uses. MEMS devices are ubiquitous in modern technologies, and can be found as fluid directors in ink-jet printers, accelerometers in mobile phones and vehicular airbags, and resonant filters and mixers in radio-frequency communications devices [1, 2].

As transistor dimensions have scaled down from microns to nanometers, so too

has there been a transition from MEMS to NEMS. Downscaling of NEMS results in devices with lower energy consumption, higher sensitivity, and denser integration opportunities. For example, NEMS relay switches with < 5 nm gaps between electrodes have been demonstrated at ultralow powers and voltages [3]. For NEMS resonators specifically, ultrathin suspended cantilevers possess several characteristics that make them promising candidates for next-generation sensors, including their high mechanical compliance, low mass, and high resonant frequency [4, 5]. Ultrathin resonators have been demonstrated for mass sensing with single-atom sensitivity [6].

2.2 Conventional methods

The downscaling of suspended NEMS structures to include thinner films and smaller nanogaps results in significant fabrication challenges. In the conventional, planar, layer-by-layer techniques developed for MEMS devices, a sacrificial layer is etched away to form the airgap that underlies a suspended structure, as shown in Figure 2-1a [2]. However, as gaps scale down, surface adhesive forces such as the van der Waals force and capillary force begin to dominate, as illustrated in Figure 2-1b; this leads to the irreversible collapse of fragile structures, particularly for the mechanically compliant ultrathin films needed to achieve next-generation NEMS [3]. Wet steps, in particular, become increasingly challenging as dimensions reduce due to the capillary force, and this common collapse mechanism reduces device yield and limits possible processes [7].

2.3 Alternative techniques

To continue the downscaling of NEMS for smaller device elements, novel concepts have been proposed for three-dimensional nanofabrication beyond the traditional planar paradigm; these include approaches based on focused ion beams (FIB), 3D printing, and kirigami. In one approach, FIB-based nanofabrication leverages a directed ion beam to either sputter away material or deposit material using gas injection. Because

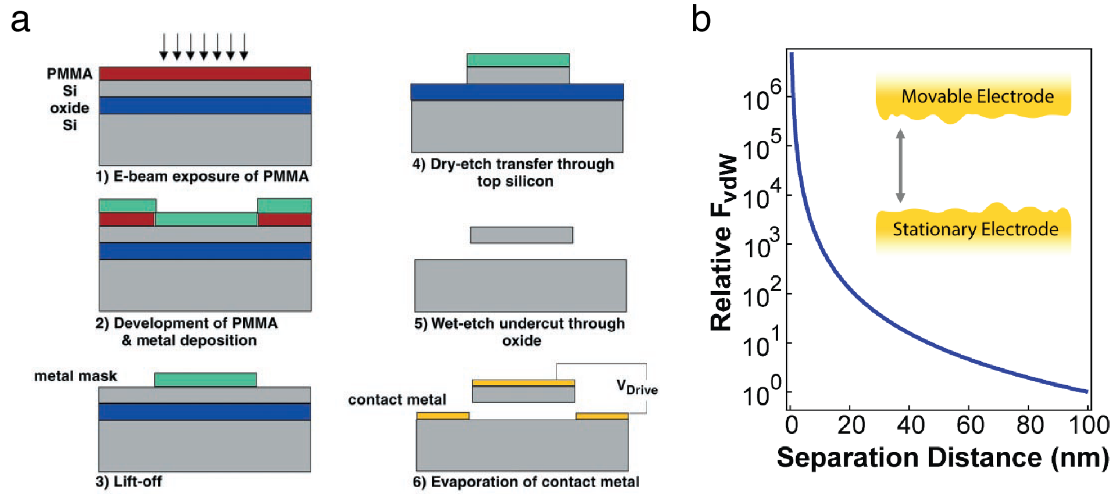

Figure 2-1: Limitations of conventional NEMS fabrication. (a) A schematic of the typical conventional technique for fabricating a suspended NEMS structure, including the sacrificial layer wet etch. From [2]. Reprinted with permission from AAAS. (b) Illustration of increasing surface forces with decreasing distance between two surfaces.

this highly focused beam can be programmatically directed in three dimensions, this technique has the capability to directly "write" matter itself in 3D (Figure 2-2a). Ion irradiation can also be used to control stress and manipulate structures. Unfortunately, this method is extremely low-throughput and high-cost due to its serial direct-write nature [8]. In another approach, 3D printing via two-photon lithography has been demonstrated for the fabrication of NEMS devices (Figure 2-2b). Two-photon printing locally polymerizes resist in a bath using the principle of multi-photon absorption at the focal point of an ultrafast laser. By directing this focal point in 3D, the polymer can be selectively cured in an arbitrary geometry with submicron resolution. This technique is severely limited in compatible materials; in addition, it suffers from the same low-throughput issues as FIB due to its direct-write nature [9]. Finally, kirigami, which transforms a 2D flat object into a 3D shape using cutting and folding, has been applied as a nanofabrication technique. This method leverages nanoscale forces such as the capillary force and residual stress to activate a directed, spontaneous transformation from a planar continuous film into a complex structure (Figure 2-2c). There remains much research to be done in applying the principles of

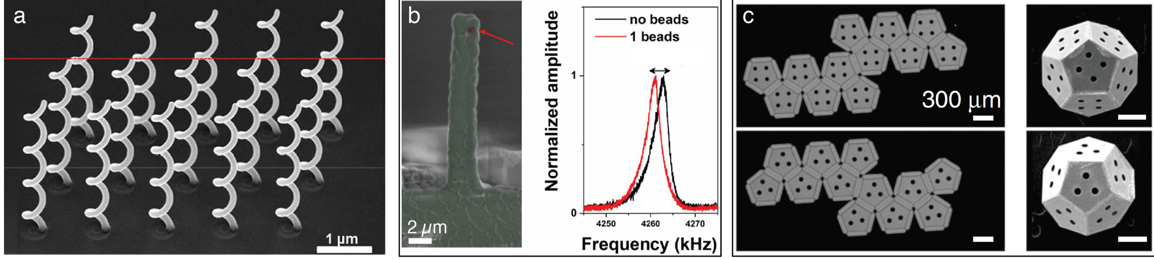

Figure 2-2: Examples of 3D features fabricated using the alternative techniques of (a) focused-ion beam deposition (Reproduced from [8] with permission from the Royal Society of Chemistry), (b) two-photon printing (Reproduced from [9]), and (c) kirigami (Reproduced from [10]).

kirigami to fabricating NEMS in useful materials systems using scalable techniques [10].

2.4 Thin-film blistering for NEMS fabrication

The buckling or blistering of thin films has been studied as a failure mechanism in thin-film coatings exposed to high temperatures. For example, unwanted blistering in films grown by atomic layer deposition (ALD) for solar cell passivation coatings has been carefully studied in an attempt to prevent this effect [11]. Only a few authors have posited the intentional utilization of thin-film blistering as a fabrication technique for electromechanical systems. Liu et al. measured the resonant frequency of randomly-forming blisters in ALD oxide stacks using piezoelectric actuation and readout by optical interferometry; however, they did not make any attempt to pattern these naturally-occurring, microscale features [12]. In a series of papers, DeCorby and colleagues demonstrate a technique for the patterning of delamination buckles in thick (micron-scale), sputtered layers of Si and SiO_2 for use as optical waveguides [13]. If this type of kirigami-inspired technique for patterned film buckling could be downscaled and applied to thin films, it could be used as an alternative fabrication method for ultrathin suspended NEMS components.

In this thesis, drawing on the principles of thin film delamination, a kirigami-inspired technique is introduced for control over the buckling of ultrathin films into

nonplanar nanostructures with deterministic spatial arrangement and tunable size. In contrast to the conventional techniques for NEMS fabrication, the proposed method is inherently stable and does not involve any sacrificial layer removal. Unlike the alternative additive manufacturing techniques of FIB and two-photon printing, the technique is high-throughput as it is compatible with the commonly used planar fabrication techniques consisting mainly of lithography, deposition and etching. Finally, in contrast to the previously studied thin-film blistering literature, the proposed strategy is both patterned and compatible with ultrathin films down to < 10 nm.

Chapter 3

Nonplanar nanofabrication method

3.1 Technique overview

To address the limitations of current methods for fabricating suspended NEMS features, we propose a technique for stable and scalable fabrication of nonplanar nanostructures by leveraging bottom-up engineering of surface interactions. In this approach, we deterministically modify the stress in a deposited thin-film and its local adhesion to a substrate, guiding delamination of planar films and their transformation into nonplanar architectures. With this platform, we extend conventional wafer-scale fabrication to yield nanometer-precise 3D features that can also be mechanically-active.

The fabrication scheme is summarized in Figure 3-1a. For a complete process description, see Appendix A. We use lithographically patterned self-assembled molecular monolayers (SAMs) to selectively modify the surface properties of a substrate. Once the patterned SAM is formed, atomic layer deposition (ALD) is used to grow a thin oxide film. Following oxide growth, the sample is annealed at 500°C for 5 minutes, inducing local oxide delamination into nonplanar nanostructures at sites defined by the SAM pattern. Figures 3-1b-d present examples of the resulting deterministic arrays of 8 nm-thin oxide nanoblisters with controlled dimensions, characterized through optical microscopy (Figure 3-1b), scanning electron microscopy (SEM) (Figure 3-1c), and atomic force microscopy (AFM) (Figure 3-1d).

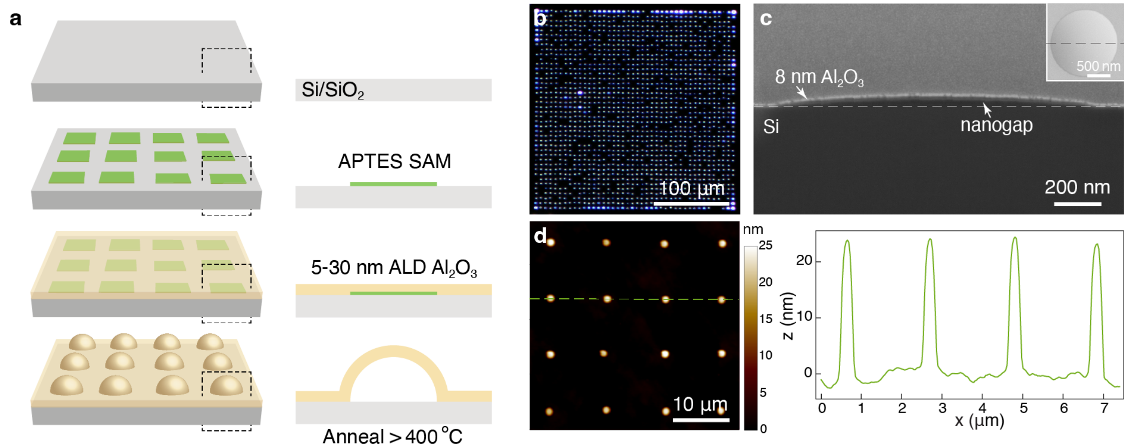

Figure 3-1: Fabrication technique overview. (a) Schematic representation of the fabrication steps. (b) Darkfield optical microscope image of an array of nonplanar nanoblisters. (c) Cross-sectional SEM of a nanoblister. (d) AFM topography (left) and line scan (right) of an array of example features.

3.2 Self-assembled molecular monolayers

3.2.1 Introduction to SAMs

Self-assembled molecular monolayers (SAMs) are one-molecule thick layers that bind to some surface in an orderly manner under appropriate conditions. They have been used for decades in applications such as biochemical sensors, where surface functionalization can be used to manipulate device interactions with chemical or biological compounds [14], or as anti-stiction coatings in MEMS [3]. The organic molecules that make up a SAM generally consist of an anchoring group that bonds to the surface; a functional tail group that sticks out towards the environment and influences the surface properties of the molecular layer; and a molecular backbone, usually a carbon chain, that connects the two. The anchoring group is chosen to allow selective assembly onto the desired surface; for example, a thiol anchoring group will bond to a gold surface, while a silane anchoring group is used to bind to oxide surfaces. The length of the carbon backbone helps determine the ultimate density of the SAM, since longer molecules will be more attracted to one another due to the van der Waals force and will thus assemble more densely [15]. The functional tail is selected based on the

desired surface functionalization, such as fluorine groups for application as a superhydrophobic coating or an amine group for bio-conjugation. Deposition methods include liquid-phase and vapor-phase techniques, and the exact deposition parameters vary based on the application, molecule, and desired properties [16].

3.2.2 Patterning of SAMs

Some applications of SAMs require patterning of the molecular layer, i.e. the ability to define molecular-functionalized regions on a substrate using some 2D mask. Several approaches have been demonstrated for this type of process, including microcontact printing using an elastomeric stamp [15], direct lithography on the SAM using electron beam or deep UV exposure [17, 18], and liftoff-based techniques [19]. We selected a liftoff technique as it is broadly applicable to diverse SAMs and is compatible with conventional fabrication processes.

Unlike conventional liftoff strategies that rely on a polymeric resist to perform the lithographic step, we developed a process using an oxide hard mask; this approach avoids polymeric residues on the surface which could influence the molecular assembly. Initially, we experimented with both photoresist and electron-beam resist masks; however, after these polymer-based masks were subjected to overnight vapor-phase SAM deposition in a vacuum desiccator, the masks became difficult to remove with solvents. For this reason and to generally promote a clean assembly, we instead pursued the oxide mask approach.

Our SAM patterning method is summarized in Figure 3-2a. To form the hard mask, first, a 2 nm-thin film of aluminum oxide, Al_2O_3, is grown on a clean Si/SiO_2 substrate using thermal ALD at 200°C with 20 alternating cycles of trimethylaluminum (TMA) and H_2O. Then, after applying a hexamethyldisilazane (HMDS) adhesion layer, a positive photoresist, AZ3312 (AZ Electronic Materials), is spincoated on top and exposed in the desired pattern through a lithography step. The photoresist developer used to develop the pattern, AZ300 (AZ Electronic Materials) contains 2.4% tetramethylammonium hydroxide (TMAH), which etches Al_2O_3. Thus, during an extended 5 minute resist development step, the oxide underlying the exposed re-

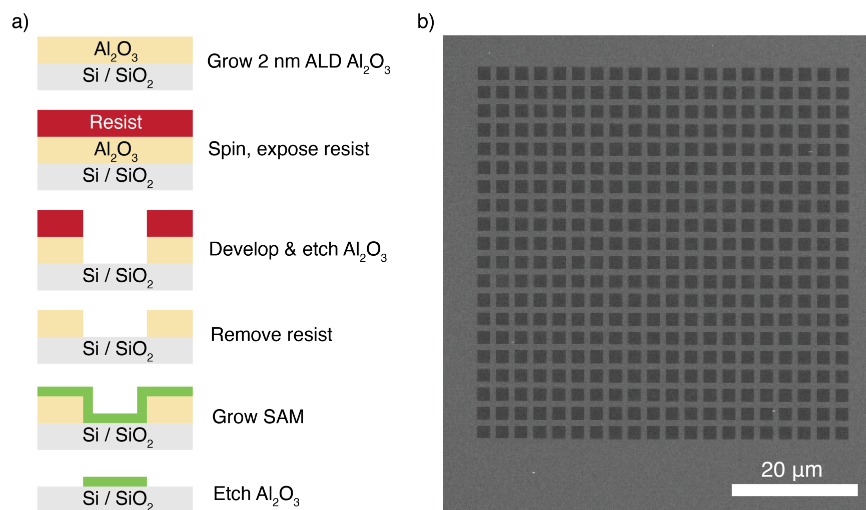

Figure 3-2: (a) SAM patterning method using an Al_2O_3 hard mask. (b) SEM image of an example Al_2O_3 hard mask prior to SAM growth. Dark squares represent bare Si while the light background represents the Al_2O_3 mask.

gions is also removed, revealing clean Si/SiO_2 that is free of organic contaminants, as the substrate has avoided direct contact with the resist. The resist is then stripped for 10 minutes in acetone, followed by two minutes of ashing in oxygen plasma. The result is a patterned Al_2O_3 mask with ultraclean Si in the exposed areas. Following assembly of the silane SAM, which assembles on both Si/SiO_2 and Al_2O_3, the sample is submersed in AZ300 TMAH developer for 5 minutes, etching away the Al_2O_3 to leave behind only the SAM regions assembled on the exposed Si/SiO_2 surface. We have found this technique to reliably pattern a clean SAM using either photolithography as described above, or electron beam lithography (EBL) for higher resolution features. To utilize the technique with EBL, Al_2O_3 deposition is followed by spincoating poly(methyl-methacrylate) (PMMA), exposing with an electron beam, developing with methyl isobutyl ketone (MIBK), and then etching the Al_2O_3 with AZ300. Prior to hard mask removal, the mask can be visualized using SEM, as demonstrated in Figure 3-2b.

3.2.3 Assembly and properties of (3-aminopropyl)triethoxysilane

The SAM used in our technique is (3-aminopropyl)triethoxysilane or APTES (Sigma Aldrich, 99%), drawn in Figure 3-3a. This is a short silane SAM with an amine functional group at the tail. As a silane, it covalently bonds to hydroxyl (−OH) groups on an oxide substrate through a hydrolysis-condensation reaction in the presence of water [16]. To promote assembly, the substrate must first be terminated with −OH groups, which act as the sites for molecule bonding. Substrate hydroxylation is accomplished using a short, low-power oxygen plasma treatment on a substrate containing physisorbed H_2O. Since a hydroxylated surface is superhydrophilic, −OH group density can be confirmed by measuring the advancing water contact angle on the substrate using a goniometer; a $1\mu L$ water drop should make a $< 2^\circ$ angle with a properly prepared substrate.

Once the substrate is prepared, APTES can be assembled in the vapor phase. The substrate is placed into a desiccator under vacuum for 12 hours along with $90\mu L$ of deionized water and $30\mu L$ of liquid molecule, each in separate containers. Water is needed to activate the hydrolysis step of the reaction [16]. The substrate(s) must be face-up in the desiccator to allow vaporized molecule to reach the surface to react and assemble. Following assembly, substrates are sonicated for 5 minutes in ethanol to remove physisorbed APTES, leaving only the chemisorbed molecular monolayer.

An important property of APTES in the context of this thesis is its thermal stability. As a gamma-substituted silane, APTES can withstand fairly high temperatures, up to 350°C in the short-term as reported by manufacturers for that class of molecule [16]. However, above these temperatures, the carbon backbone breaks apart, resulting in molecular decomposition. We measured the thermal stability of an APTES monolayer by using a goniometer to measure the advancing water contact angle of an APTES-functionalized Si surface after 5 minute anneals at varying temperatures. Contact angle, which provides information about the surface energy, is a good indication of the SAM quality. As demonstrated in Figure 3-3b, the contact angle of APTES remains stable up to about 200°C, after which it progressively decreases until

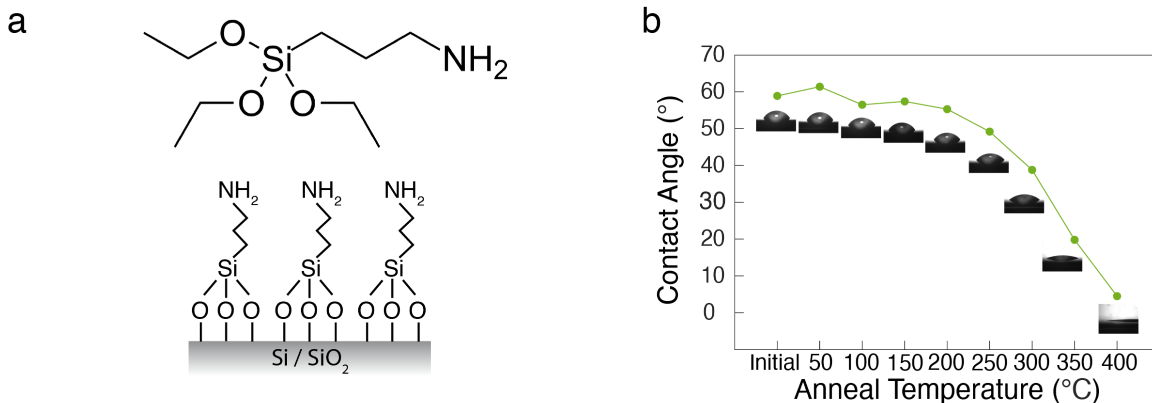

Figure 3-3: (a) Schematic of (3-aminopropyl)triethoxysilane, or APTES (top) and illustration of its assembly on an oxide-terminated Si surface (bottom). (b) The water contact angle of APTES after 5 minute anneals at varying temperatures, indicating the degradation of the molecule at temperatures above 200°C. Goniometer images of droplets used in the measurement are shown as inset.

the molecule is completely degraded at 400°C.

3.3 Atomic layer deposition

3.3.1 ALD chemistry

Atomic layer deposition (ALD) is a chemical vapor deposition technique for growing highly uniform, conformal thin films with atomic precision. A sample is placed into a deposition chamber under vacuum, and is sequentially exposed to pulses of precursor gases which react with the surface in a self-limiting manner to grow some film on the substrate, atomic layer by atomic layer. ALD can use heat or plasma to provide the energy needed to induce these reactions.

In the case of thermal ALD, the growth of Al_2O_3 from trimethylaluminum (TMA) and H_2O precursors is considered a model system. This process is illustrated in Figure 3-4. In this reaction, TMA, with formula $Al(CH_3)_3$, acts as the metal source and H_2O as the oxidizing counter-reactant. During the first half-reaction, TMA chemisorbs to $-$OH groups present on the sample surface, producing CH_4 as a byproduct; the sample is exposed to TMA long enough for each surface $-$OH group to react,

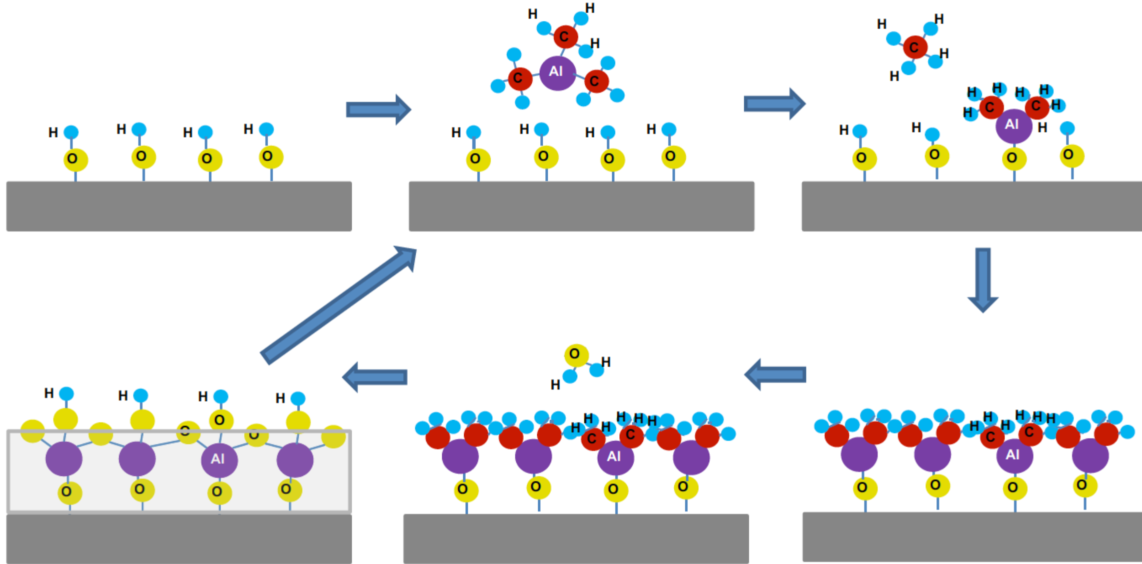

Figure 3-4: An illustration of the typical TMA/H_2O process for ALD of Al_2O_3 on a hydroxyl-functionalized surface. Reproduced from [21].

and then residual TMA and byproducts are removed by pumping. For the second half-reaction, H_2O is introduced to the chamber, reacting with the surface to remove methyl groups and producing CH_4 and H_2 byproducts, before residual precursor and byproducts are pumped away. At this stage, Al_2O_3 is left behind on the sample surface, freshly functionalized with new $-$OH groups for the subsequent TMA half-reaction. The A/B cycle can be repeated an arbitrary number of times to grow an amorphous Al_2O_3 film with precise thickness proportional to the number of cycles. A recipe optimized to operate within the layer-by-layer "ALD window" should grow about 1.0 Å/cycle [20].

3.3.2 ALD growth on molecules

Since ALD growth is so dependent on substrate surface chemistry, surface functionalization via SAMs has been heavily investigated as a way to control ALD. While plasma-activated ALD can in general produce higher-quality metal oxide films due to the high reactivity and easy purging of O_2 plasma as compared to H_2O, we expect that the plasma will also destroy organic molecules that might be present on a sample, so we focus on thermal ALD for our process. The thermal ALD temperature should

be set high enough to place the recipe within the ALD window, but low enough to avoid destroying the molecules.

The majority of research on SAM-mediated ALD thus far has focused on patterning SAMs that block ALD growth to achieve area-selective deposition. For the ALD-blocking application, the SAM anchoring group is chosen to assemble on the appropriate substrate, the carbon chain is long to promote dense assembly, and the functional tail group is selected to inhibit ALD precursor chemisorption and thus prevent film growth. In the case of ALD of metal oxides, the most common type of molecule selected for blocking has been CH_3-terminated SAMs with backbones of 8 or more carbon atoms, such as octyltrichlorosilane (OTS) or octadecyltrichlorosilane (ODTS). However, ALD of Al_2O_3 is very hard to block due to the high reactivity of the TMA precursor, so other metal oxide ALD processes such as HfO_2 are typically used, as shown in Figure 3-5a-c [15]. To block ALD of Al_2O_3, superhydrophobic fluorine-terminated SAMs have been shown to be slightly more effective than CH_3-terminated SAMs, as demonstrated in Figure 3-5d [22].

Much less studied is the use of SAMs which intentionally provide sites for covalent bonding of ALD precursors to initiate growth on the SAM itself. Xu and Musgrave [23] performed a theoretical study on the growth of Al_2O_3 using a thermal TMA/H_2O process on top of SAMs with varying surface terminations. They analyze the reaction mechanism of TMA chemisorbing on $-OH$, $-NH_2$, and $-CH_3$-terminated SAMs using density functional theory. These authors find that an $-OH$ surface provides the most energetically favorable reaction with the fastest rate. The $-NH_2$ termination still provides a favorable reaction, illustrated in Figure 3-6, but with an energy barrier double that of the $-OH$ case, meaning that this reaction would require a temperature above 300°C to proceed at the same rate as in the $-OH$ case. Since this temperature is above the thermal degradation point of the SAM as discussed in section 3.2.3, a more feasible deposition scenario at 200°C would result in faster ALD growth for an $-OH$ surface than an $-NH_2$ surface unless the initial exposure to TMA was substantially lengthened. A $-CH_3$-terminated SAM, on the other hand, does not provide an energetically favorable reaction mechanism to covalently bond to TMA; the overall

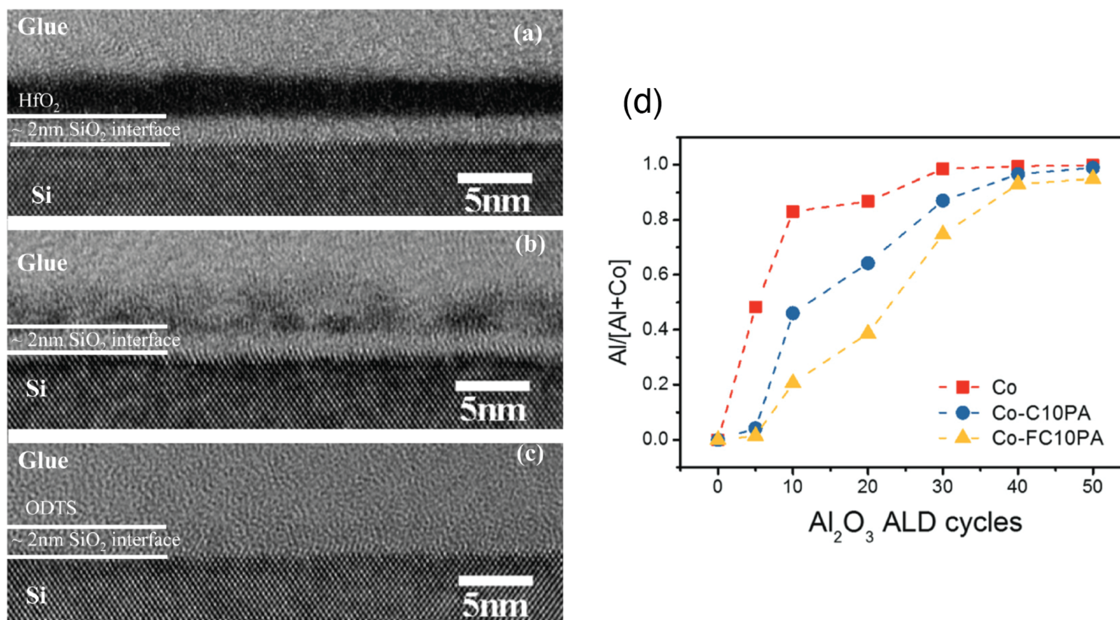

Figure 3-5: Literature demonstrations of SAMs used for ALD blocking. (a-c) Cross-sectional TEM images demonstrating blocking of HfO_2 ALD using CH_3-terminated SAMs; (a) has no SAM functionalization and HfO_2 grows readily, (b) uses a medium-length SAM (OTS) and partially blocks HfO_2, and (c) uses a long SAM (ODTS) and effectively blocks HfO_2. Reprinted with permission from [15]. Copyright 2009 American Chemical Society. (d) XPS composition analysis (atomic percentage of Al) indicating blocking of Al_2O_3 ALD on a Cobalt surface by an alkyl SAM (C10PA) and fluoroalkyl SAM (FC10PA). The fluorine-terminated SAM blocks more effectively than the CH_3-terminated SAM. Reproduced from [22] with permission from the Royal Society of Chemistry.

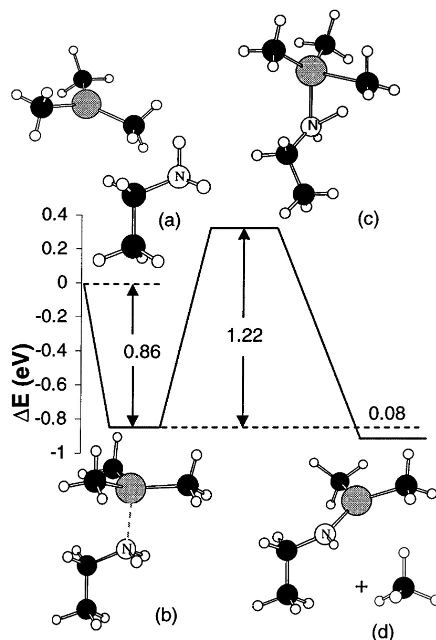

Figure 3-6: Reaction pathway for the bonding of a TMA precursor molecule to an $-NH_2$ termination. The reaction path and predicted energies were identified using density functional theory calculations. Reprinted with permission from [23]. Copyright 2004 American Chemical Society.

enthalpy of reaction is endothermic, thus there is no thermodynamic driving force for this reaction to occur [23]. Al_2O_3 will not grow on a methyl-terminated SAM unless the precursors nucleate on some defect/contaminant or break through the SAM to reach the underlying substrate, which is why these $-CH_3$ SAMs are often used for ALD-blocking applications [15]. However, due to the high reactivity of TMA, this precursor will eventually break through a $-CH_3$-terminated SAM and nucleate on the substrate after some cycles. Although the Xu and Musgrave paper did not address fluorine-terminated SAMs, based on available literature, these should act similarly to the $-CH_3$ SAMs, but with even more cycles of ALD resistance [22].

Räupke et al. [24] provide experimental evidence via quartz crystal microbalance data, photoluminescence (PL) data, and x-ray photoelectron spectroscopy data for the covalent bonding of the aluminum atom in TMA to the nitrogen atom in the $-NH_2$ termination of APTES, supporting the theoretical analysis by Xu and Musgrave [23]. They grow an APTES SAM on an Al_2O_3 substrate, then expose to TMA to

form the Al-N covalent bonds, followed by exposure to 8-HQ molecules which react with TMA to form Alq_3, which emits strongly at 524 nm. To validate the reaction mechanism, they compare PL of the resultant surface with and without the initial APTES functionalization, where the version without APTES emits much more weakly than the version with APTES, as expected for an amine-less version of the compound. Therefore, strong evidence is provided for the covalent Al-N bond formation between TMA and APTES during ALD [24].

We provide additional experimental support for the theory on TMA bonding to various surface terminations. Figure 3-7 demonstrates the thickness of Al_2O_3 measured by optical ellipsometry after 80 identical cycles of TMA/H_2O thermal ALD at 200°C on three Si/SiO_2 substrates, each with a different surface functionalization. The three surface terminations were: (1) the superhydrophobic fluorinated SAM perfluorodecyltriethoxysilane (PFDTES), (2) an APTES SAM (amine-terminated), and (3) a surface which has been densely hydroxylated (-OH) using weak oxygen plasma treatment in the presence of water. The OH-termination produced the thickest Al_2O_3 layer with an ideal ALD deposition rate of 1.0 Å/cycle; the NH_2-termination produced a 4% thinner Al_2O_3 layer; and the fluorine termination generated a 9% thinner layer. These results support the theory that $-NH_2$ supports covalent ALD growth although at a slower reaction rate than -OH, as predicted by Xu and Musgrave [23]; additionally, PFDTES blocked ALD for the most number of cycles out of the three terminations, but did eventually allow precursors to break through to the substrate and begin to grow oxide.

3.3.3 Discussion

Section 3.3 has presented theoretical arguments and experimental evidence that when ALD of Al_2O_3 is performed on an APTES-functionalized surface, the initial TMA precursor molecules covalently bond to the molecule's terminal amine group, and the reaction proceeds on top of the APTES layer from there. This implies that the resultant oxide layer experiences an adhesion to the underlying substrate which is mediated by the APTES molecular layer. In our process, a substrate with patterned

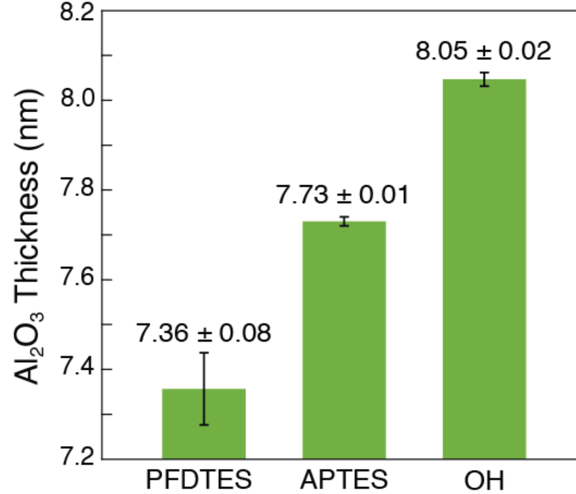

Figure 3-7: Experimental results demonstrating ellipsometric measurements of Al_2O_3 film thickness after 80 ALD cycles on substrates with varying surface functionality. -OH grows Al_2O_3 readily, while the NH_2-terminated APTES grows Al_2O_3 more slowly, as predicted by [23]. The fluoroalkyl PFDTES blocks ALD for the most number of cycles, but the ALD precursors eventually break through the molecular layer to nucleate and initiate growth on the substrate surface.

APTES functionalization is subjected to thermal ALD of Al_2O_3 at 200°C. We have demonstrated that APTES can easily withstand this temperature without degrading (Figure 3-3b, section 3.2.3). Thus, based on available evidence, we posit that our ALD-on-patterned-APTES process results in an oxide layer with high adhesion to the substrate in non-APTES regions and APTES-controlled adhesion to the substrate in APTES-coated regions. Later, the APTES can be intentionally degraded in order to release the oxide layer from the substrate in the APTES-functionalized areas, allowing for lithographic control over high and low adhesion areas in the oxide film. The implications of this are critical to the proposed technique and will be discussed in Section 3.4.

3.4 Controlled film buckling

As discussed in Section 3.3, an underlying patterned APTES layer enables spatial control over the adhesion of an ALD Al_2O_3 film to a substrate. This spatial adhesion control can be leveraged in combination with control over film stress to produce non-

planar delamination buckles in the oxide film in predetermined locations and with predetermined geometry; this is the core mechanism of the proposed technique. Critically, the key changes in adhesion and film stress are both activated simultaneously using a high-temperature (> 400°C) anneal. This anneal thermally degrades the APTES by breaking apart its carbon chain (Figure 3-3b, section 3.2.3), releasing the oxide film from the substrate in APTES-coated regions. At the same time, due to the mismatch in thermal expansion coefficients between the film and substrate, the film builds up compressive thermal stress, triggering the formation of circular delamination buckles or blisters to relieve the stress. These blisters form preferentially in areas where oxide-substrate adhesion is low; that is, the now-degraded APTES-functionalized regions. Therefore, the localization of the nonplanar features is controlled by the APTES pattern. As we will see in the following subsections, the size of these features can also be well-controlled by the geometric parameters of the lithographic mask used to pattern the APTES.

3.4.1 Thermal stress in thin films

The deposition temperature of ALD, in our case 200°C, sets the equilibrium state of the film, since it is during deposition that the chemical bonds are formed within the oxide and between the oxide and substrate. Thus, the film experiences thermal stress at any temperature besides the deposition temperature due to the difference in thermal expansion coefficients between the film and the substrate. After the initial film growth at 200°C, the sample is removed from the ALD chamber into a room-temperature environment. As the film and substrate cool, the film wants to contract more than the substrate does, since the thermal expansion coefficient of Al_2O_3 is larger than that of Si. Since the thickness of the substrate is much larger than the thickness of the film, the substrate is unaffected and the size mismatch expresses itself as tensile stress in the film.

When the sample is annealed to 500°C during the subsequent fabrication step, the opposite effect occurs; due to its higher coefficient of thermal expansion, the film wants to expand more than the substrate, causing it to build up significant

Table 3.1: Material parameters for thin ALD Al_2O_3 and bulk Si used in calculations throughout section 3.4, from [27].

$E_{Al_2O_3}$	$\nu_{Al_2O_3}$	α_{Si}	$\alpha_{Al_2O_3}$
170 GPa	0.24	$3.0 \times 10^{-6} °C^{-1}$	$4.2 \times 10^{-6} °C^{-1}$

compressive stress.

The expression for the thermal stress in an Al_2O_3 thin film on a silicon substrate is given by equation 3.1 [25]:

$$\sigma_{thermal} = \frac{E_{Al_2O_3}}{1 - \nu_{Al_2O_3}} (\alpha_{Si} - \alpha_{Al_2O_3})(T_1 - T_0) \tag{3.1}$$

where $\sigma_{thermal}$ is the film stress, $E_{Al_2O_3}$ is the elastic modulus of thin ALD Al_2O_3, $\nu_{Al_2O_3}$ is its Poisson ratio, α_{Si} and $\alpha_{Al_2O_3}$ are the respective thermal expansion coefficients for Si and Al_2O_3, T_0 is the deposition temperature (200°C), and T_1 is the ambient temperature. The sign convention for stress is that $\sigma > 0$ is tensile while $\sigma < 0$ is compressive. This model is valid if the film and the substrate have similar elastic moduli, which is the case here since $E_{Si} = 180$ GPa [26] and $E_{Al_2O_3} = 170$ GPa [27]. All the relevant material parameter values for the case of thin ALD Al_2O_3 on Si are given in table 3.1. Equation 3.1 is plotted in Figure 3-8 where the thin-film stress can be visualized as a function of the ambient temperature, demonstrating positive (tensile) stress at cooler temperatures and negative (compressive) stress at warmer temperatures.

3.4.2 Modeling of thin film buckling

When a film is in a high-stress state, including from thermal stress due to a mismatch of thermal expansion coefficients, some transformation will occur to relieve the stress. In the case where the adhesion between the film and substrate is very good, this may take the form of plastic deformation, micro-cracking, or viscous flow in the thin film. In the case where the adhesion between substrate and film is poor, the stress relief mechanism may take the form of cracking in the tensile case or buckle-driven

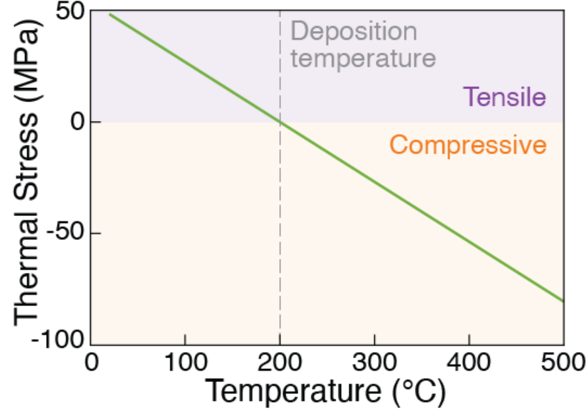

Figure 3-8: Plot of thermal stress in an ALD Al_2O_3 film grown at 200°C on Si as a function of the ambient temperature. Uses equation 3.1 and material parameters from table 3.1.

delamination in the compressive case. For compressed films, common buckling modes include the straight-sided blister, circular blister, and "telephone cord" morphologies [28].

Hutchinson and Suo [28] analyze the mechanics of the circular blister case as a failure mode in compressed thin films. This analysis models the circular delaminated region of the film as a buckled plate and the blister edge as a semi-infinite edge crack on an interface. They use the von Karman nonlinear plate equations to model the axisymmetric deformation of a clamped circular plate. These equations can be solved analytically if the buckling deflection is sufficiently small, which is the treatment followed here. The relevant geometric dimensions used in the following equations are illustrated in Figure 3-9.

First, the critical buckling stress of a clamped circular plate is

$$\sigma_c = 1.2235 \frac{E_{Al_2O_3}}{1 - \nu_{Al_2O_3}^2} \left(\frac{t}{r} \right)^2 \tag{3.2}$$

where $E_{Al_2O_3}$ and $\nu_{Al_2O_3}$ are the elastic modulus and Poisson ratio of the film (the model is general but an Al_2O_3 film is specified for consistency across this chapter), t is the film thickness, and r is the radius of the circular blister. For a film experiencing stress σ_{buckle} prior to buckling, the vertical deflection δ of the blister is given by

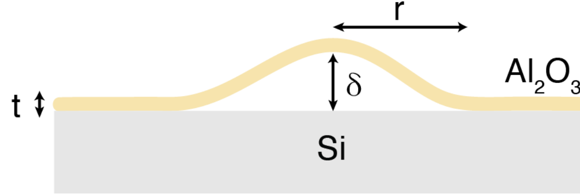

Figure 3-9: Illustration of a two-dimensional circular delamination buckle (blister) with the relevant geometric dimensions labeled.

$$\delta = t\sqrt{\frac{1}{c_1}\left(\frac{\sigma_{buckle}}{\sigma_c} - 1\right)} \tag{3.3}$$

where $c_1 = 0.2473(1+\nu) + 0.2231(1-\nu^2)$ is a constant that is a function of the Poisson ratio. Rearranging equation 3.3 to solve for σ_{buckle} gives

$$\sigma_{buckle} = \sigma_c\left(c_1\left(\frac{\delta}{t}\right)^2 + 1\right) \tag{3.4}$$

which, in combination with equation 3.2, represents the stress relieved by a circular blister with radius r and vertical deflection δ in a film with thickness t, elastic modulus E, and Poisson ratio ν [28].

To demonstrate that the force exerted by thermal stress across an area of film is equal to the force required to deform the corresponding blister, the thermal stress and buckling stress can be integrated and compared. Since stress is given in units of $Pa = \frac{N}{m^2}$, integrating stress across an area gives force: $\frac{N}{m^2} * m^2 = N$. For a lithographic mask where the APTES SAM is present on square islands with side-length s separated by spacing p, the film area accounted for by each blister is an $s+p$ by $s+p$ square. This is illustrated in Figure 3-10a. Therefore, the thermal force accounted for by each blister is

$$F_{thermal} = \sigma_{thermal} * (s+p)^2 \tag{3.5}$$

Similarly, the buckling stress σ_{buckle} can be integrated across the horizontal area πr^2 (where r is the blister radius) occupied by the blister (Figure 3-10b) in order to give the total force relieved by blistering:

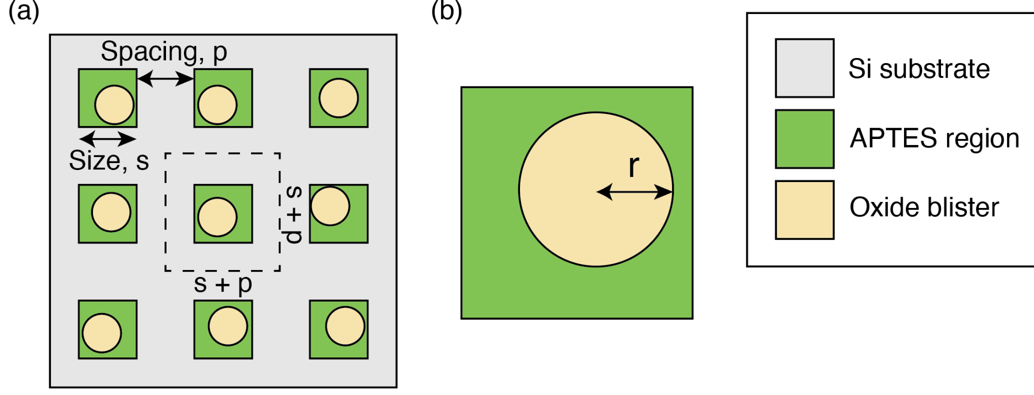

Figure 3-10: Illustration of the geometric dimensions used in equation 3.5 and equation 3.6. (a) An array of patterned blisters where size s is the width of the APTES-functionalized regions and spacing p is the distance between consecutive APTES-functionalized regions. Each blister accounts for the thermal stress in a square region around it with side-length $s + p$, as indicated by the dashed box. (b) The resultant blisters that form within the APTES-functionalized regions have radius r.

$$F_{buckle} = \sigma_{buckle} * \pi r^2 \tag{3.6}$$

To demonstrate the validity of this explanation for the blistering effect, these two forces should be empirically shown to be equal. This is accomplished in subsection 3.4.3.

By setting $F_{thermal} = F_{buckle}$ and assuming for now that δ depends linearly on r such that $\delta = m * r + b$ where m and b are constants, we can rearrange and combine equations 3.1 - 3.6 to obtain an expression for the blister radius

$$r = \frac{1}{m}\left(\sqrt{\frac{1}{c_1}\left(\frac{\sigma_t(s+p)^2(1-\nu^2_{\mathrm{Al_2O_3}})}{1.2235\pi * E_{\mathrm{Al_2O_3}}} - t^2\right)} + b\right) \tag{3.7}$$

where radius r is a function of the material parameters and temperature conditions, blister height, film thickness, and APTES size and spacing. Subsection 3.4.3 will compare this relation to empirical results.

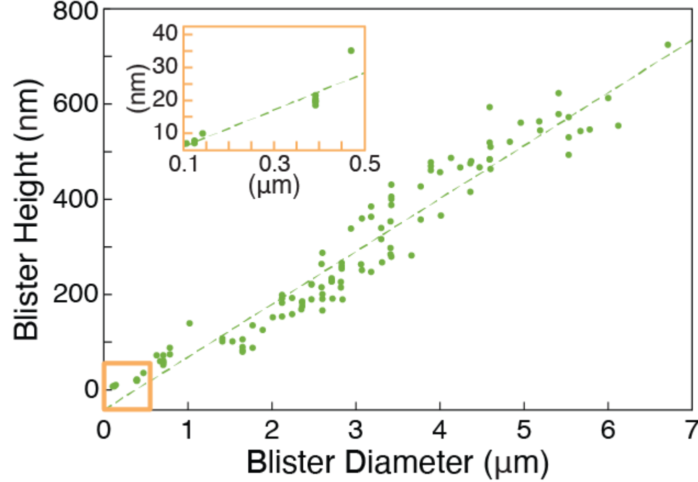

Figure 3-11: The height (δ) of a blister is plotted against its diameter. Each data point represents an individual blister. The inset emphasizes the smallest blisters demonstrated, with nanogaps of down to 7 nm. The height/diameter ratio is a constant, with the linear regression line plotted on top of the data.

3.4.3 Empirical results

To characterize our nanofabrication process, an experiment was performed using an 8 nm-thin layer of Al_2O_3 on patterned APTES annealed at 500°C. The APTES was patterned using photolithography for features larger than $2\mu m$ and electron-beam lithography for features smaller than $2\mu m$. APTES was patterned into arrays of squares where the size of and spacing between APTES-functionalized regions were varied between arrays. Characterization of the blister dimensions was performed using a combination of optical microscopy and atomic force microscopy (AFM).

First, the relationship between blister height δ and blister diameter was characterized. Data was collected using AFM. Figure 3-11 plots the results, where each data point represents an individual blister. The inset shows a zoomed-in plot of the smallest features measured, where the nanogap size reaches down to 7 nm, dimensions that would be very challenging to fabricate reliably at scale using conventional techniques. Linear regression on the height vs. radius data reveals a fit of $\delta = 0.222 * r - 0.0424$ where δ and r are in μm and $R^2 = 0.936$.

Figure 3-12 presents the average diameter of blisters formed in an array against the size of patterned APTES regions and spacing between them. Data was collected

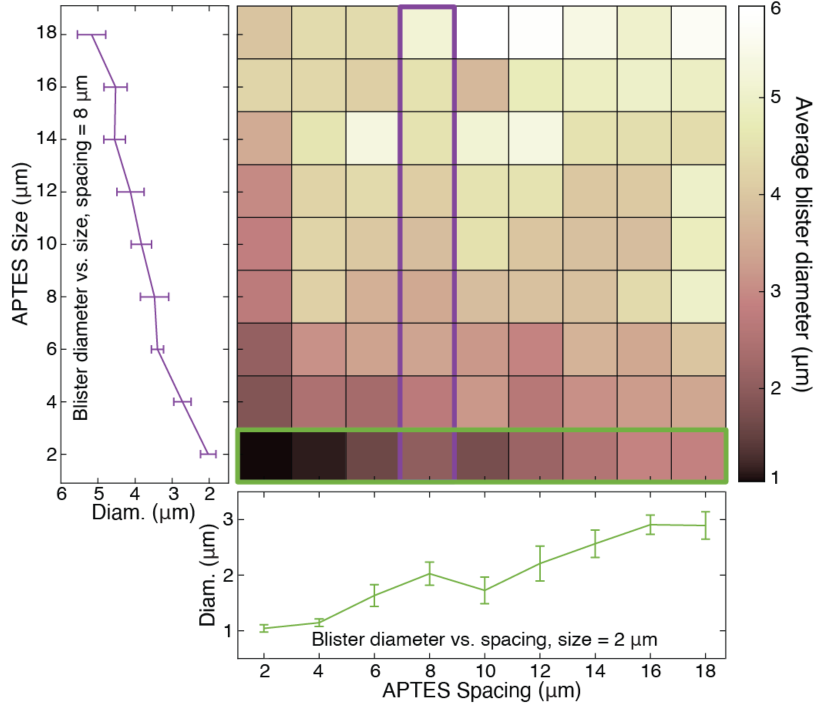

Figure 3-12: The average blister diameter is plotted as a heatmap against the two lithographic mask parameters, APTES size and APTES spacing. The two adjacent line plots represent blister diameter plotted against APTES size and APTES spacing respectively, while holding the other constant at a selected value.

using optical microscopy images of 81 arrays of blisters (9 sizes, 9 spacings). The blister diameters were extracted from optical images using the MATLAB function $imfindcircles$ in the MATLAB Image Processing Toolbox. This function implements a circular Hough transform to identify circles in an image.

As Figure 3-12 demonstrates, there is a positive relationship between both the size s and spacing p of APTES regions and the resulting blister diameter. This supports the theory that blistering is due to the buildup of thermal compressive stress across an $s + p$ by $s + p$ area. In order to further probe this theory, the same data was replotted in Figure 3-13 to visualize blister radius vs. APTES size + spacing. The empirical data is compared to an overlaid plot of equation 3.7 to compare the actual radius to that predicted by the theoretical model.

To support the assumption that the force due to thermal stress, $F_{thermal}$, accounts for the force relieved by the blister, $F_{blister}$, the empirical results for $F_{thermal}$ and

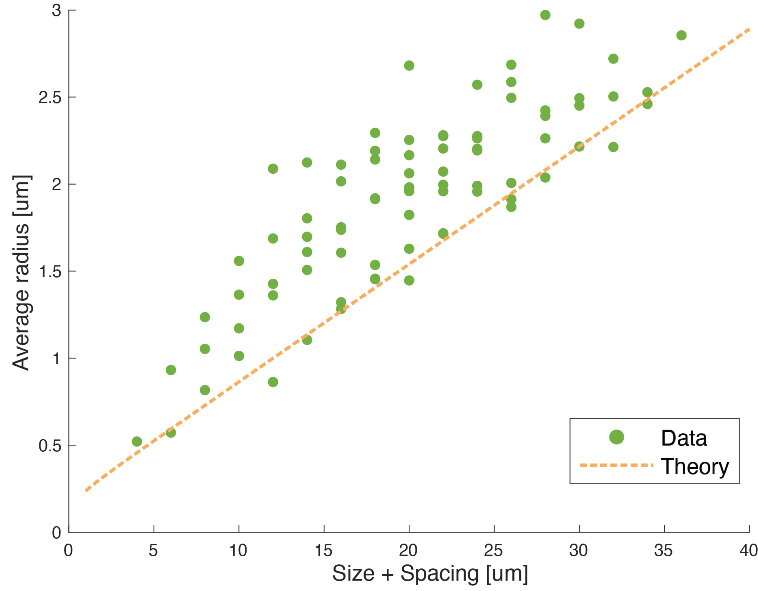

Figure 3-13: The average blister radius for a given combination of APTES region size + spacing is plotted in green, while the theoretical value based on equation 3.7 is overlaid in orange.

$F_{blister}$ are plotted in Figure 3-14 based on plugging in empirical data to equations 3.5 and 3.6. Also included is a linear regression fit to the data with 95% confidence bounds, as well as a line demonstrating what the fit should look like if the hypothesis that $F_{blister} = F_{thermal}$ is true.

3.4.4 Discussion

As evidenced by Figure 3-13 and Figure 3-14, thermal stress plays a significant role in blister formation, although a slight mismatch between $F_{blister}$ and $F_{thermal}$ indicates an additional source of stress present during annealing, perhaps due to some small degree of crystallization occurring during the annealing process [27]. Regardless, we can conclude that the thermal stress accounts for the majority of buckling stress and that the trends and orders of magnitude of the model presented are correct.

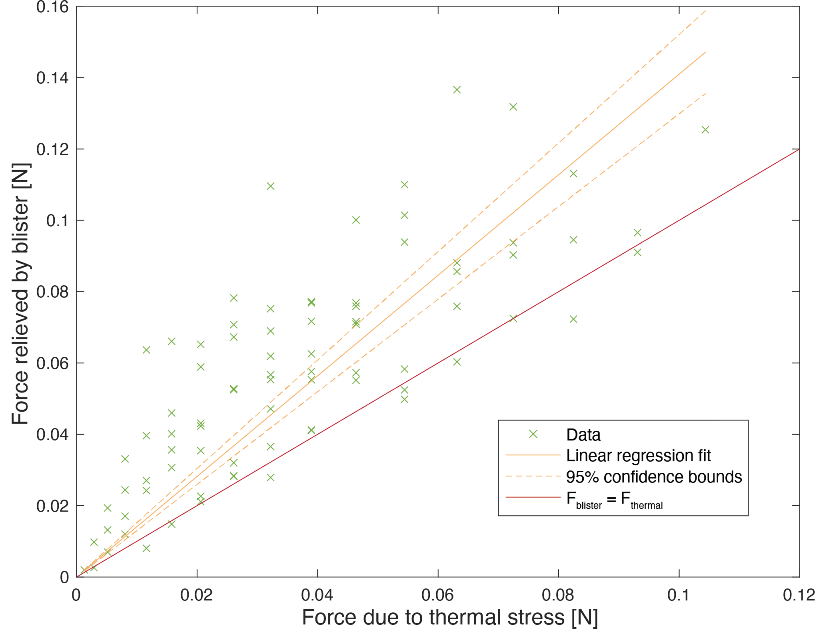

Figure 3-14: The blistering force $F_{blister}$ is plotted against the thermal force $F_{thermal}$ by plugging empirical blister dimensions and APTES geometry into the force equations. A linear fit plus confidence intervals for the data is shown, plus a line indicating what the fit should look like if $F_{blister} = F_{thermal}$.

3.5 Material compatibility

Our platform is not limited to the Al_2O_3-on-silicon materials system discussed so far, and can be extended to other substrates and deposited thin-films. We have demonstrated our technique with diverse substrates including tungsten, silicon, silicon nitride and hafnium oxide. While in this work we used substrates that are compatible with silane-based molecular self-assembly, i.e., oxides and oxide-terminated metals, different SAM anchoring group chemistries could accommodate alternative substrates.

Additionally, a compatible substrate must be able to withstand the high temperatures used during the anneal step; the key material parameter here is the recrystallization temperature of the substrate material. Materials with low recrystallization temperatures will rearrange their surface atoms when annealed, disrupting the engineered stress in the thin film and rendering the process unreliable. We have observed this phenomenon in metals such as gold and aluminum, with recrystallization temperatures of 200°C [29] and 150°C [30] respectively, but not in tungsten, with a

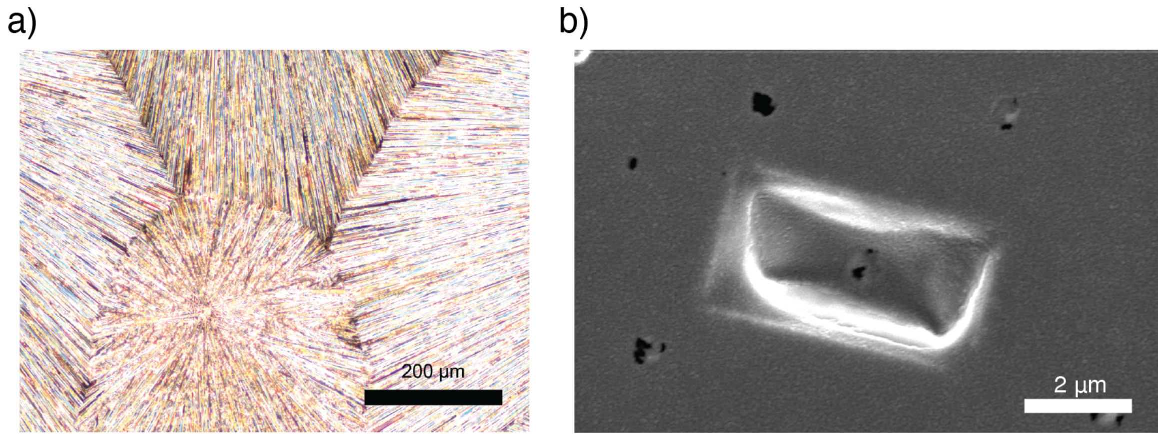

Figure 3-15: The impact of metal substrate recrystallization after annealing at 500°C for 5 minutes. (a) Optical image of recrystallized Au. (b) SEM image of an artifact formed in recrystallized Al.

recrystallization temperature of 1200°C [30]. Figure 3-15 shows images of recrystallized Au and Al after anneals at 500°C. To avoid this issue, alternative molecules and thin-film membrane materials may be used that enable the process to work at lower anneal temperatures.

For the oxide film, besides Al_2O_3, we have also demonstrated our fabrication process with ALD HfO_2. We expect that the thin-film can be further extended to other materials, as long as (1) the deposited material forms a continuous film on the SAM surface without causing its degradation or breaking through to adhere to the substrate, and (2) the resulting film has a larger coefficient of thermal expansion than the substrate to help initiate delamination during annealing. As applied to ALD, point (1) above necessitates a relatively gentle ALD process; we anticipate that plasma-activated ALD processes and ALD at temperatures above the degradation point of the SAM would be unsuccessful. Additionally, the ALD chemistry must be compatible with the SAM end group such that it is thermodynamically favorable for the ALD film to grow on top of the SAM. For this, alternative molecular layers that meet the needs of the desired materials systems might be necessary.

Figure 3-16 shows example optical images of the results of our process performed with a variety of substrates and thin-film materials, demonstrating the technique's versatility. We expect that this process could also be extended to non-oxide thin films

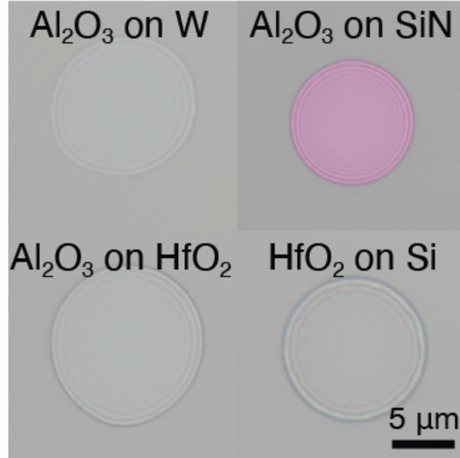

Figure 3-16: Optical images demonstrating the technique with different substrate and thin-film materials.

deposited through a variety of strategies including and beyond ALD. This will be a topic of our future studies.

3.6 Scalable fabrication of a mechanical resonator

An important feature of our technique for forming nonplanar nanostructures is that these structures are stable enough to undergo subsequent processing to further transform their morphologies. Specifically, we have demonstrated the extension of our technique to form ultrathin double-clamped bridge structures that could be used as mechanical resonators. The resonator characterization is discussed in detail in the next section.

The fabrication steps for the bridge structures are summarized in Figure 3-17. We begin with a substrate containing arrays of our circular blisters, whose fabrication is discussed in detail earlier in this chapter. Next, we spin-coat resist, lithographically expose, and develop; we have primarily utilized electron-beam lithography (EBL) and the EBL resist poly(methyl methacrylate) (PMMA) for this purpose, but high-resolution photolithography could easily be used. After lithography, the regions left unprotected by resist are the sides of the circular blisters; the central region of the blister which will become the bridge remains protected by the resist. Next, we use

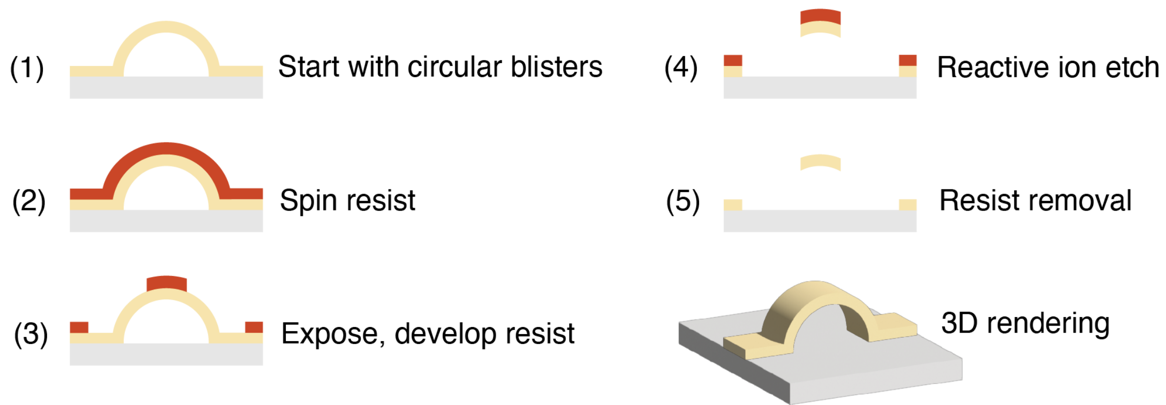

Figure 3-17: Fabrication steps for converting the nanoblister to a bridge geometry.

a reactive ion etch (RIE) to anisotropically etch the portions of the thin film left exposed, i.e. the sides of the circular blisters. In our experiments, we use a chlorine-based RIE to etch the Al_2O_3 thin film, but an alternative RIE chemistry could be applied to an alternative thin film material. PMMA is removed from the sample by soaking in an acetone bath. The sample is transferred to isopropyl alcohol while still wet with acetone, and then dried in a critical point dryer (CPD) in order to prevent structural collapse during drying. CPD is a technique which manipulates temperature and pressure during the drying process in order to dry the sample at the critical point between liquid and gas phases, thereby eliminating surface tension forces during drying. CPD becomes necessary after the interior of the blister has been exposed by the RIE, since capillary action can now contribute to structural collapse during drying. Finally, PMMA residues are removed using an oxygen plasma etch.

The result of this process is large arrays of ultrathin, suspended, double-clamped oxide beams, fabricated using wafer-scale techniques. Example SEM images of the structures are shown in Figure 3-18.

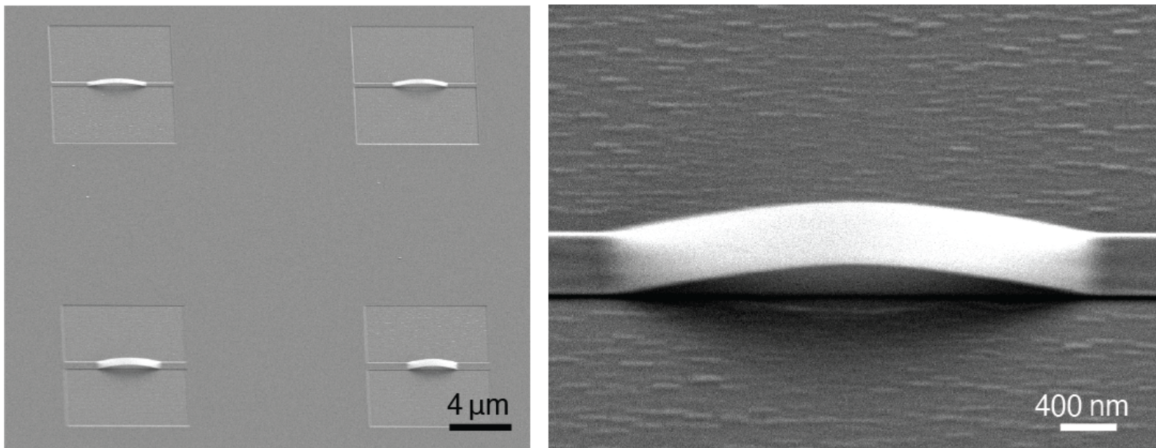

Figure 3-18: SEM images of examples of bridge nanostructures fabricated using the discussed technique.

Chapter 4

Mechanical resonator and characterization

4.1 Mass spectroscopy application

One promising application of the ultrathin suspended films discussed in chapter 3 is in mechanical resonators, primarily in the realm of sensing via mass spectroscopy. Resonant mass spectroscopy is a technique in which the shift in resonant frequency of a mechanical resonator is used to determine the mass of some particle that has physically adhered to the resonator. This method is utilized in biology and chemistry for the detection and identification of single cells or molecules [31], and even in physics for the detection of single atoms [6].

The resonant frequency ω of some vibrating object can be expressed to first order using the equation $\omega = \sqrt{\frac{k}{m}}$, where k represents the spring constant or restoring force and m is the mass. A change in mass results in a corresponding shift in the resonant frequency, which can then be measured by readout electronics and used to calculate the added mass. The sensitivity of the mass spectrometer is largely determined by the mass of the resonator itself, since a lower initial mass means a change in mass has a larger impact on the resonant frequency. Additionally, operating at a high resonant frequency increases sensitivity, since changes in frequency can be more easily detected.

Low-mass, high-frequency resonant spectrometers have been demonstrated in sil-

Table 4.1: Material parameters for thin ALD Al_2O_3 used in the finite element modeling, from [27].

Young's modulus	Poisson ratio	Density
$170GPa$	0.24	$3.05g/cm^3$

icon with sensitivities up to 87.8 Hz per attogram [32], and a carbon nanotube resonator demonstrated mass sensitivity of 7700 Hz per attogram [6]. Moreover, reducing the built-in stress within a resonant mass spectrometer improves reproducibility, sensitivity, and tunability [5]. Therefore, important figures of merit for a resonator to be used in mass spectroscopy are low mass, high resonant frequency, and low built-in stress. In this chapter, I demonstrate that the nanostructures fabricated through the proposed technique are excellent candidates in all three metrics.

4.2 Finite element modeling

Due to the unique curved shape of the nonplanar nanostructures, analytical modeling of resonance is complex. In order to model the vibrational resonant modes of a circular blister or bridge, COMSOL Multiphysics software was used to create a mechanics simulation. An ellipsoid shell was used to model the shape of the curved thin film, where the oxide was modeled as a linear elastic material constrained to be fixed at the intersection with the substrate. Material parameters for the oxide are taken from [27] and presented in table 4.1. This simulation assumes that the resonator is free of built-in stress, which we hypothesize to be true since the blister formation itself is a stress-relief mechanism. To find the vibrational resonant modes, an eigenfrequency study was used.

Figure 4-1 shows the first four vibrational mode shapes for canonical examples of the blister and bridge geometries, as visualized by COMSOL simulation. For the blister geometry, the mode shapes compare favorably with those shown in the literature for low-stress circular membranes [33]. For the bridge geometry, the lowest two vibrational resonances correspond well with the widely accepted resonant shapes

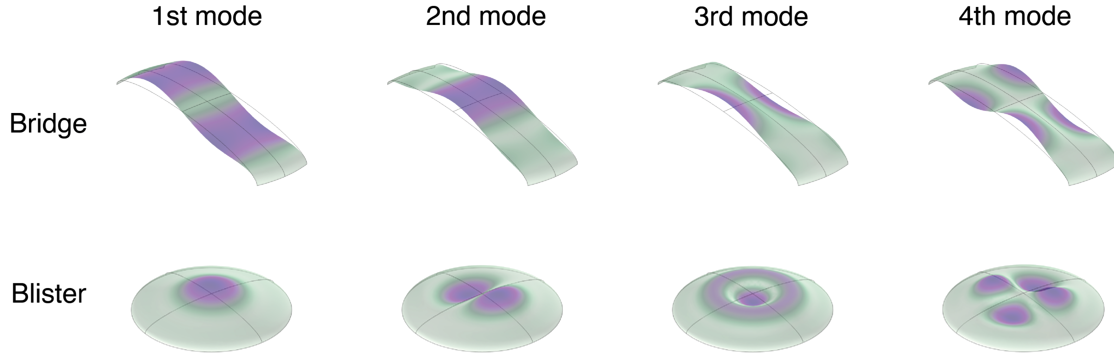

Figure 4-1: Shapes of the first four vibrational modes for the canonical blister and bridge geometries, generated in COMSOL.

for the double-clamped beam, but higher modes diverge due to the unique aspect ratios in the ultrathin bridge.

Using COMSOL, geometric parameters were varied and the resultant fundamental frequency recorded, in order to establish a relationship between different aspects of the nanostructure shape and the vibrational properties. Based on the empirical relation found in section 3.4.3, the height was assumed based on $\delta = 0.222 * r - 0.0424$. For the circular blister geometry, film thickness was swept from 5 nm - 30 nm, while blister radius was held constant at $1\mu m$; then, film thickness was held constant at 10 nm while blister radius was swept from $0.25\mu m$ - $10\mu m$. Finally, for the bridge geometry, film thickness was held constant at 10 nm and blister radius was held at $5\mu m$, while the bridge width was swept from $0.1\mu m$ to $5\mu m$. Note that for the bridge, radius represents the size of the blister used to form the bridge. The results of these simulations are presented in Figure 4-2.

These simulations can be interpreted as different methods of varying the spring constant, aka stiffness or restoring force of the resonator. A thicker film, smaller blister, and wider bridge all effectively increase the spring constant k, thereby increasing the resonant frequency $\omega = \sqrt{\frac{k}{m}}$. As can be seen in Figure 4-2, varying the blister radius has the largest effect on resonance, followed by varying the film thickness; varying the bridge width has the least effect on the fundamental frequency. However, the bridge width does have a major effect on the mode shape; narrower bridges will

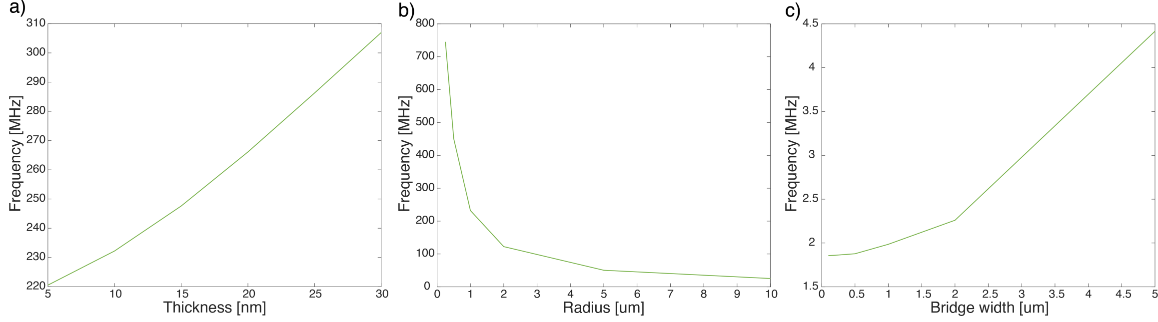

Figure 4-2: Dependence of resonator fundamental frequency on geometric parameters, from COMSOL simulation. (a) Film thickness of a circular blister is varied, with radius = $1\mu m$. (b) Radius of a circular blister is varied, with film thickness = 10 nm. (c) Width of a bridge structure is varied, with radius = $5\mu m$ and thickness = 10 nm.

have their resonant vibrations concentrated towards the center of the structure, while wider bridges have their perturbations concentrated towards the free edges.

4.3 Empirical characterization

As an initial demonstration of the potential of our technique to fabricate ultrathin, low-stress, high frequency resonators, we measured the mechanical frequency response of an example bridge structure in collaboration with Jian Zhou and David Czaplewski at Argonne National Laboratory. The resonator was measured in vacuum at 10^{-6} Torr to reduce air damping and increase the setup sensitivity. We utilized a home-built laser interferometer, schematized in Figure 4-3 [5], to characterize the deflection amplitude of the bridge center in response to sinusoidal actuation from an underlying piezoelectric stage as well as the non-actuated response from thermomechanical noise. The measurement works by interfering the two paths of light that result from a 632.8 nm HeNe laser beam incident on the resonant suspended membrane; first, the portion of the beam that reflects off of the film, and second, the portion which passes through the film and reflects off of the substrate wafer below. As the mechanical actuation frequency approaches the device resonance, the membrane deflects with a larger amplitude, changing the relative path length between the suspended film and the substrate. The interference caused by this change in path length is measurable

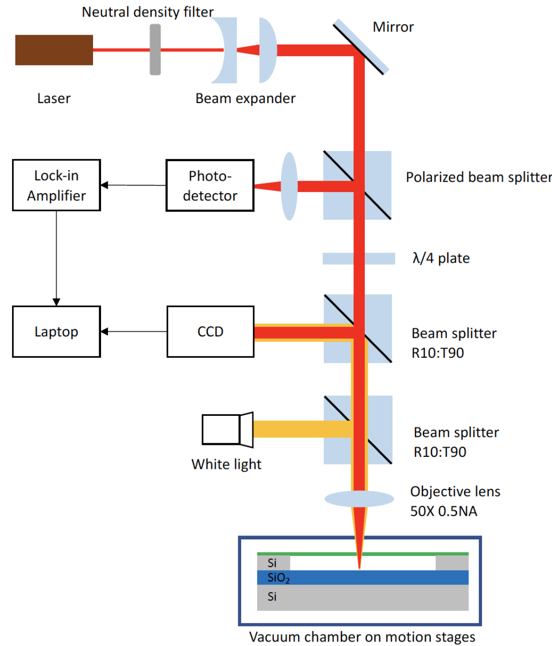

Figure 4-3: The laser interferometer setup used in the experiment. Reprinted with permission from [5]. Copyright 2020 American Chemical Society.

by the interferometer via a photodetector (New Focus 1801 FS) and lock-in amplifier (Zurich Instruments HF2LI), and a quantity proportional to the deflection amplitude can be measured at each input frequency.

The example bridge used in the measurement had a length of $31.58\mu m$, width of $10.77\mu m$, and film thickness 31.398 nm. Length and width were measured using SEM, while film thickness was measured with ellipsometry. The blister height was assumed based on the linear fit from section 3.4.3. Figure 4-4 shows an SEM of the structure measured, the interferometer-measured frequency response with different actuation amplitudes as well as the non-actuated thermomechanical noise response, and the COMSOL simulation of the 2nd vibrational mode of the structure based on its measured dimensions. The 2nd mode was used since it is the mode that results in a deflection at the center of the bridge, where the interferometer laser was focused. The measurement shows excellent agreement with simulation, where a resonant frequency of 1.2688 MHz was measured and the simulated value was 1.2685 MHz, implying a discrepancy of only 0.02%. This degree of agreement between experiment and simulation suggests that the resonator has extremely low built-in stress, since built-

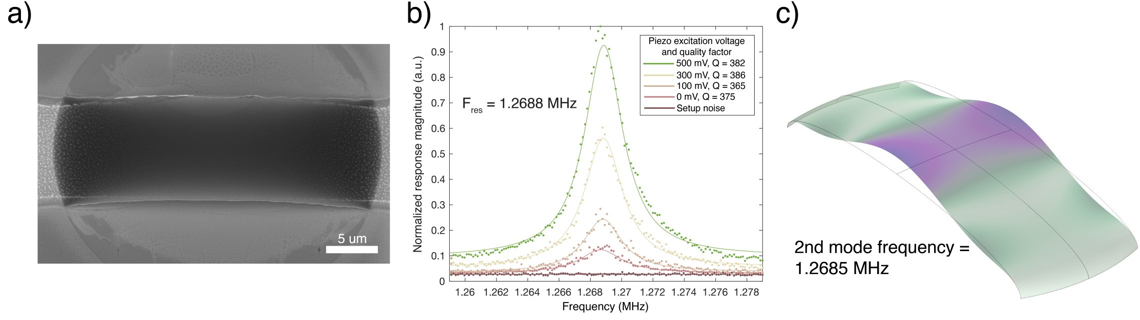

Figure 4-4: The example bridge resonator characterized. (a) SEM image of the device. (b) Empirical characterization of mechanical frequency response, including the system noise, thermomechanical noise measurement of frequency, and several piezo-actuated responses at increasing piezo amplitudes. (c) COMSOL simulation of the 2nd resonant mode of the device measured.

in stress would significantly shift the resonant frequency and the simulation assumed zero stress. Additionally, measurement indicated a quality factor of around 380, which is within the expected range for an amorphous oxide resonator [5].

The mass of the resonator is estimated at 3.26×10^{-11}g which implies an effective spring constant $k = 52.4\frac{g}{s^2}$ based on $\omega = \sqrt{\frac{k}{m}}$. This would suggest a sensitivity of the resonant frequency to added mass of 0.0195 Hz per attogram.

4.4 Discussion

The figures of merit for a resonant mass spectrometer discussed in section 4.1 were low mass, high resonant frequency, and low built-in stress. The preliminary device we measured resonated in the MHz range with a mass on the order of 1×10^{-11}g, suggesting a mass sensitivity of 0.0195 Hz per attogram. This sensitivity should improve for smaller devices which resonate at higher frequencies. For example, an 8 nm-thick, $1\mu m$-long and $0.25\mu m$-wide device is expected to resonate at 186 MHz with a mass of 6.10×10^{-15}g, implying mass sensitivity of 15244 Hz per attogram, almost twice as sensitive as the state-of-the-art carbon nanotube mass spectrometer in [6]. Optimizing our experimental setup to accommodate measurements of smaller, higher-frequency resonators is an ongoing focus of our work. Finally, it is important to note that the close agreement (0.02% deviation) of our measured resonance value with the

stress-free simulated value suggests that our resonators have very low built-in stress; we expect that this is due to the stress relief-based fabrication mechanism. This is important for device reproducibility and sensitivity [5]. Overall, our technique shows great promise for developing scalable, nanoscale mechanical resonators with superior performance for mass spectroscopy, which we are investigating in ongoing work.

Chapter 5

Conclusion and future work

This work has presented a new fabrication strategy for the development of suspended nonplanar nanostructures for applications in nanoelectromechanical devices. This is accomplished through engineering of local surface forces and material stresses which enable bottom-up transformation of planar features into nonplanar designs. In doing so, we move beyond the conventional CMOS paradigm of lithography-deposition-etch to achieve device geometries that are challenging to realize using the traditional methods, leveraging the unique forces found at the nanoscale instead of working against them.

We have demonstrated a technique which is simple, reproducible, scalable, and compatible with diverse materials. Using a single wafer-scale lithography step, we can produce nonplanar designs in dense arrays across large areas. While we focused primarily on a single materials system for proof-of-concept, the technique can establish a general platform where substrates, thin-film materials, and molecules can be mixed and matched to achieve the desired properties.

Additionally, we have shown preliminary data suggesting the application of our devices as low-mass, high frequency resonators with potential use as ultrasensitive mass spectrometers. The device measured is notable for the coincidence of its empirical resonant frequency with the simulated value, indicating that it may have particularly low built-in strain, which is useful for increasing device reproducibility and sensitivity. Our ongoing work is focused on experimental characterization of smaller, lower-mass,

and higher-frequency devices that are expected to achieve higher sensitivities. In the future, these resonators could also be integrated into systems to perform multiplexed mass spectroscopy and sensing with high resolution across dense resonator arrays, with applications in chemistry and biology.

Overall, the technique presented here can help push the boundaries of NEMS fabrication towards the few-nanometers dimensions to realize diverse devices, including switches, memory cells, resonators, actuators, and sensors with improved energy-efficiency, sensitivity, and operating speed. Additionally, the method may enable new opportunities for emerging applications in computing surfaces, metamaterials, and quantum devices. In the words of Richard Feynman, through bottom-up nanofabrication strategies, we continue to find "plenty of room at the bottom" for improved electronic devices that solve real human problems.

Appendix A

Fabrication parameters

The details of the device fabrication are presented here.

A.1 Substrate preparation

1. Coat an Si or SiO_2 on Si (University Wafer) substrate with resist and dice into pieces, then rinse with acetone.
2. Sonicate twice in acetone, 2 minutes each.
3. Boil twice in IPA, 2 minutes each.
4. Ash 2 minutes in oxygen plasma cleaner.

A.2 Oxide hard mask

1. Grow 2 nm of Al_2O_3 using 20 cycles of thermal ALD (TMA/H_2O) at 200°C (Cambridge Nanotech, Savannah 200).
2. Apply HMDS resist adhesion layer (YES Oven), 10 second recipe.
3. Spincoat AZ3312 photoresist (MicroChemicals): 500 rpm for 6 seconds, 750 rpm fo 6 seconds, 3000 rpm for 30 seconds.

4. Soft bake resist, 100°C for 1 minute.

5. Expose resist using 375 nm laser at 140 mJ/cm^2 (Heidelberg MLA150).

6. Post bake 110°C, 90 seconds.

7. Develop 300 seconds, AZ300 developer (MicroChemicals), gently agitate. Submerge in DI water, 30 seconds.

8. Resist removal: rinse with acetone, soak in acetone 10 minutes, swirl in IPA, dry with nitrogen gun.

A.3 APTES growth and hard mask removal

1. Clean resist residues with oxygen plasma ash, 2 minutes.

2. Apply DI water to substrate and dry with nitrogen (to add physisorbed water), then hydroxylate using low-power 10 second oxygen plasma ash.

3. Place sample face-up in vacuum desiccator for 12 hours with 90μL DI water and 30μL (3-aminopropyl)triethoxysilane (Sigma Aldrich, 99%), each in their own open dish.

4. After 12 hours, remove sample from desiccator and sonicate 5 minutes in ethanol to remove physisorbed molecule.

5. Liftoff hard mask in AZ300 developer (MicroChemicals), 5 minutes. Rinse in DI water 30 seconds.

A.4 Thin-film growth and blistering

1. Grow 5-30 nm of Al_2O_3 using 50-300 cycles of thermal ALD (TMA/H_2O) at 200°C (Cambridge Nanotech, Savannah 200).

2. Anneal at 500°C, 5 minutes.

A.5 Etching blisters into double-clamped beams

1. Spincoat PMMA 950K A3 (MicroChem) at 1500 rpm, 45 seconds.

2. Soft bake at 180°C, 2 minutes.

3. Expose with electron beam lithography, 2 nA current, 1400 μC/cm^2 dose (Elionix F125).

4. Develop 90 seconds in mixture of 1 mL MIBK (Kayaku) and 3 mL IPA, then rinse twice in IPA for 2 minutes each.

5. RIE etch (SAMCO ICP etcher): chamber preconditoning with NF_3 clean twice for 120 seconds each at 40°C, then chlorine clean twice for 10 minutes each at 40°C, then etch with chlorine-based Al_2O_3 recipe for 3.5 seconds per nanometer oxide.

6. Remove resist in acetone (10 minutes), then transfer while wet to IPA, and critical point dry (Tousimis Autosamdri-931).

7. Clean resist residues with oxygen plasma ash for 5 minutes.

Bibliography

[1] J. Basu and T. K. Bhattacharyya, "Microelectromechanical resonators for radio frequency communication applications," *Microsystem Technologies*, vol. 17, pp. 1557–1580, Aug. 2011.

[2] H. G. Craighead, "Nanoelectromechanical Systems," *Science*, vol. 290, pp. 1532–1535, Nov. 2000.

[3] F. Niroui, A. I. Wang, E. M. Sletten, Y. Song, J. Kong, E. Yablonovitch, T. M. Swager, J. H. Lang, and V. Bulović, "Tunneling Nanoelectromechanical Switches Based on Compressible Molecular Thin Films," *ACS Nano*, vol. 9, pp. 7886–7894, Aug. 2015.

[4] X. Li, T. Ono, Y. Wang, and M. Esashi, "Study on ultra-thin NEMS cantilevers - high yield fabrication and size-effect on Young's modulus of silicon," in *Technical Digest. MEMS 2002 IEEE International Conference. Fifteenth IEEE International Conference on Micro Electro Mechanical Systems (Cat. No.02CH37266)*, pp. 427–430, Jan. 2002.

[5] J. Zhou, N. Moldovan, L. Stan, H. Cai, D. A. Czaplewski, and D. López, "Approaching the Strain-Free Limit in Ultrathin Nanomechanical Resonators," *Nano Letters*, vol. 20, pp. 5693–5698, Aug. 2020.

[6] K. Jensen, K. Kim, and A. Zettl, "An atomic-resolution nanomechanical mass sensor," *Nature Nanotechnology*, vol. 3, pp. 533–537, Sept. 2008.

[7] F. Niroui, E. M. Sletten, P. B. Deotare, A. I. Wang, T. M. Swager, J. H. Lang, and V. Bulović, "Controlled fabrication of nanoscale gaps using stiction," in *2015 28th IEEE International Conference on Micro Electro Mechanical Systems (MEMS)*, pp. 85–88, Jan. 2015.

[8] P. Li, S. Chen, H. Dai, Z. Yang, Z. Chen, Y. Wang, Y. Chen, W. Peng, W. Shan, and H. Duan, "Recent advances in focused ion beam nanofabrication for nanostructures and devices: fundamentals and applications," *Nanoscale*, vol. 13, pp. 1529–1565, Jan. 2021.

[9] S. Stassi, I. Cooperstein, M. Tortello, C. F. Pirri, S. Magdassi, and C. Ricciardi, "Reaching silicon-based NEMS performances with 3D printed nanomechanical resonators," *Nature Communications*, vol. 12, p. 6080, Oct. 2021.

[10] S. Chen, J. Chen, X. Zhang, Z.-Y. Li, and J. Li, "Kirigami/origami: unfolding the new regime of advanced 3D microfabrication/nanofabrication with "folding"," *Light: Science & Applications*, vol. 9, p. 75, Dec. 2020.

[11] B. Vermang, H. Goverde, V. Simons, I. De Wolf, J. Meersschaut, S. Tanaka, J. John, J. Poortmans, and R. Mertens, "A study of blister formation in ALD Al_2O_3 grown on silicon," in *2012 38th IEEE Photovoltaic Specialists Conference*, pp. 001135–001138, June 2012.

[12] H. Liu, S. Guo, R. B. Yang, C. J. J. Lee, and L. Zhang, "Giant Blistering of Nanometer-Thick Al_2O_3/ZnO Films Grown by Atomic Layer Deposition: Mechanism and Potential Applications," *ACS Applied Materials & Interfaces*, vol. 9, pp. 26201–26209, Aug. 2017.

[13] E. Epp, N. Ponnampalam, W. Newman, B. Drobot, J. N. McMullin, A. F. Meldrum, and R. G. DeCorby, "Hollow Bragg waveguides fabricated by controlled buckling of Si/SiO_2 multilayers," *Optics Express*, vol. 18, pp. 24917–24925, Nov. 2010.

[14] A. Ulman, "Formation and Structure of Self-Assembled Monolayers," *Chemical Reviews*, vol. 96, pp. 1533–1554, Jan. 1996.

[15] X. Jiang and S. F. Bent, "Area-Selective ALD with Soft Lithographic Methods: Using Self-Assembled Monolayers to Direct Film Deposition," *The Journal of Physical Chemistry C*, vol. 113, pp. 17613–17625, Oct. 2009.

[16] B. Arkles, "Silane Coupling Agents," *Gelest, Inc.*, 2014.

[17] M. J. Lercel, G. F. Redinbo, F. D. Pardo, M. Rooks, R. C. Tiberio, P. Simpson, H. G. Craighead, C. W. Sheen, A. N. Parikh, and D. L. Allara, "Electron beam lithography with monolayers of alkylthiols and alkylsiloxanes," *Journal of Vacuum Science & Technology B: Microelectronics and Nanometer Structures*, vol. 12, pp. 3663–3667, Nov. 1994.

[18] J. M. Calvert, "Lithographic patterning of self-assembled films," *Journal of Vacuum Science & Technology B: Microelectronics and Nanometer Structures*, vol. 11, pp. 2155–2163, Nov. 1993.

[19] S. Walheim, R. Müller, M. Sprenger, E. Loser, J. Mlynek, and U. Steiner, "Patterning Self-Assembled Monolayers on Oxide Surfaces Using a Lift-off Technique," *Advanced Materials*, vol. 11, pp. 1431–1433, Nov. 1999.

[20] J. L. van Hemmen, S. B. S. Heil, J. H. Klootwijk, F. Roozeboom, and C. J. Hodson, "Plasma and Thermal ALD of Al_2O_3 in a Commercial 200 mm ALD Reactor," *Journal of The Electrochemical Society*, pp. 165–169, May 2007.

[21] A. E. Marquardt, E. M. Breitung, T. Drayman-Weisser, G. Gates, and R. J. Phaneuf, "Protecting silver cultural heritage objects with atomic layer deposited corrosion barriers," *Heritage Science*, vol. 3, p. 37, Dec. 2015.

[22] C.-W. Chang, H.-H. Hsu, C.-S. Hsu, and J.-T. Chen, “Achieving area-selective atomic layer deposition with fluorinated self-assembled monolayers,” *Journal of Materials Chemistry C*, vol. 9, pp. 14589–14595, Sept. 2021.

[23] Y. Xu and C. B. Musgrave, “A DFT Study of the Al_2O_3 Atomic Layer Deposition on SAMs: Effect of SAM Termination,” *Chemistry of Materials*, vol. 16, pp. 646–653, Feb. 2004.

[24] A. Räupke, F. Albrecht, J. Maibach, A. Behrendt, A. Polywka, R. Heiderhoff, J. Helzel, T. Rabe, H.-H. Johannes, W. Kowalsky, E. Mankel, T. Mayer, P. Görrn, and T. Riedl, “Conformal and Highly Luminescent Monolayers of Alq_3 Prepared by Gas-Phase Molecular Layer Deposition,” *ACS Applied Materials & Interfaces*, vol. 6, pp. 1193–1199, Jan. 2014.

[25] S.-H. Jen, S. M. George, R. S. McLean, and P. F. Carcia, “Alucone Interlayers to Minimize Stress Caused by Thermal Expansion Mismatch between Al_2O_3 Films and Teflon Substrates,” *ACS Applied Materials & Interfaces*, vol. 5, pp. 1165–1173, Feb. 2013.

[26] M. A. Hopcroft, W. D. Nix, and T. W. Kenny, “What is the Young’s Modulus of Silicon?,” *Journal of Microelectromechanical Systems*, vol. 19, pp. 229–238, Apr. 2010.

[27] O. M. E. Ylivaara, X. Liu, L. Kilpi, J. Lyytinen, D. Schneider, M. Laitinen, J. Julin, S. Ali, S. Sintonen, M. Berdova, E. Haimi, T. Sajavaara, H. Ronkainen, H. Lipsanen, J. Koskinen, S.-P. Hannula, and R. L. Puurunen, “Aluminum oxide from trimethylaluminum and water by atomic layer deposition: The temperature dependence of residual stress, elastic modulus, hardness and adhesion,” *Thin Solid Films*, vol. 552, pp. 124–135, Feb. 2014.

[28] J. W. Hutchinson and Z. Suo, “Mixed Mode Cracking in Layered Materials,” in *Advances in Applied Mechanics* (J. W. Hutchinson and T. Y. Wu, eds.), vol. 29, pp. 63–191, Elsevier, Jan. 1991.

[29] J.-H. Cho, H.-P. Ha, and K. H. Oh, “Recrystallization and grain growth of cold-rolled gold sheet,” *Metallurgical and Materials Transactions A*, vol. 36, pp. 3415–3425, Dec. 2005.

[30] R. M. Brick, A. W. Pense, and R. B. Gordon, *Structure and Properties of Engineering Materials*. McGraw-Hill, 4th ed., 1977.

[31] F. Pujol-Vila, R. Villa, and M. Alvarez, “Nanomechanical Sensors as a Tool for Bacteria Detection and Antibiotic Susceptibility Testing,” *Frontiers in Mechanical Engineering*, vol. 6, July 2020.

[32] E. Sage, M. Sansa, S. Fostner, M. Defoort, M. Gély, A. K. Naik, R. Morel, L. Duraffourg, M. L. Roukes, T. Alava, G. Jourdan, E. Colinet, C. Masselon, A. Brenac, and S. Hentz, “Single-particle mass spectrometry with ar-

rays of frequency-addressed nanomechanical resonators," *Nature Communications*, vol. 9, p. 3283, Aug. 2018.

[33] A. Lima-Rodriguez, A. Gonzalez-Herrera, and J. Garcia-Manrique, "Study of the Dynamic Behaviour of Circular Membranes with Low Tension," *Applied Sciences*, vol. 9, p. 4716, Jan. 2019.